



# Laser Powder Bed Fusion and Heat Treatment of an AlCrFe<sub>2</sub>Ni<sub>2</sub> High Entropy Alloy

Dimitrios Vogiatzief<sup>1\*</sup>, Alper Evirgen<sup>1</sup>, Sergej Gein<sup>2</sup>, Veronica Rocio Molina<sup>3</sup>,  
Andreas Weisheit<sup>3</sup> and Mikkel Pedersen<sup>1</sup>

<sup>1</sup> Oerlikon AM GmbH, Feldkirchen, Germany, <sup>2</sup> Access e.V., Aachen, Germany, <sup>3</sup> Fraunhofer-Institut für Lasertechnik ILT, Aachen, Germany

## OPEN ACCESS

### Edited by:

Sheng Guo,  
Chalmers University of Technology,  
Sweden

### Reviewed by:

Zhang Hui,  
Anhui University of Technology, China  
Igor Moravcik,  
Brno University of Technology,  
Czechia

### \*Correspondence:

Dimitrios Vogiatzief  
dimitrios.vogiatzief@oerlikon.com

### Specialty section:

This article was submitted to  
Structural Materials,  
a section of the journal  
Frontiers in Materials

**Received:** 28 May 2020

**Accepted:** 07 July 2020

**Published:** 28 July 2020

### Citation:

Vogiatzief D, Evirgen A, Gein S,  
Molina VR, Weisheit A and  
Pedersen M (2020) Laser Powder  
Bed Fusion and Heat Treatment of an  
AlCrFe<sub>2</sub>Ni<sub>2</sub> High Entropy Alloy.  
Front. Mater. 7:248.  
doi: 10.3389/fmats.2020.00248

Recent research in the Al-Co-Cr-Fe-Ni and Al-Cr-Fe-Ni systems has shown that novel duplex materials composed of FCC and BCC phases can be obtained. Among them, alloys with a composition close to AlCrFe<sub>2</sub>Ni<sub>2</sub> retain their structural properties while being Co-free. Their strength and ductility can be tailored by adjusting the phase fractions of FCC and BCC phases, while the latter is undergoing a spinodal decomposition into ordered and disordered BCC phases. Further improvement of the properties is expected with the use of novel processing techniques such as laser powder bed fusion. This process stands out due to high geometric complexity capabilities, a wide range of accessible processing parameters, and high cooling rates that support microstructure refinement. Within the frame of the present study, alloy powder around the composition AlCrFe<sub>2</sub>Ni<sub>2</sub> was produced and coupons for material characterization were built with laser powder bed fusion. In this paper, the following will be presented: (i) prealloyed powder properties, (ii) laser powder bed fusion processing of the material, (iii) heat treatments and their subsequent effect on microstructure, and (iv) mechanical properties obtained by three-point bending and microhardness tests. A highlight of this study is the novel pathway to obtain an ultrafine duplex microstructure, which forms upon heat treatment from a metastable as-built microstructure. A spinodally decomposed BCC microstructure, retained due to solidification under high cooling rates, is used to nucleate and grow FCC micro-platelets during a subsequent heat treatment step. This ultrafine duplex material cannot be obtained under conventional processing; thus, it can be considered a unique additive manufacturing material. In the context of the heat treatment study carried out in the present work, the influence of heat treatment parameters on the phase fraction of FCC platelets and the resulting hardness and flexural properties will be discussed. Finally, the current challenges concerning the processing of the alloy and the possible optimization paths for best material performance will be discussed.

**Keywords:** laser powder bed fusion, high entropy alloy, AlCrFe<sub>2</sub>Ni<sub>2</sub>, baseplate preheating, heat treatment, duplex microstructure, BCC, FCC

## INTRODUCTION

Over the past two decades, research on High Entropy Alloys (HEAs) has intensified. The term HEA is widely used in the literature to describe alloys with unusual compositions consisting of multiple principle elements. The origin of the naming comes from the high configurational entropy that these alloys exhibit when the concentration of their constituting elements is near-equimolar according to the Boltzmann's hypothesis (Yeh et al., 2004; Yeh, 2006). Multiple systems have been investigated, with some of them exhibiting excellent compression properties (Zhou et al., 2007), high hardness (Kao et al., 2009), wear and corrosion resistance (Poletti et al., 2017; Nair et al., 2018). Based on their properties, HEAs have been characterized as interesting candidates for numerous applications. HEAs consisting of 3d transition metals showed mechanical properties comparable to Ni alloys and various grades of stainless steels, e.g., austenitic or duplex stainless steels (Miracle and Senkov, 2017), making them promising for structural applications. One of the most studied HEA systems is Al-Co-Cr-Fe-Ni. Alloys within this system consist of solid solution phases, e.g., Body-Centered Cubic (BCC), Face-Centered Cubic (FCC), or both, depending on the Al concentration or Al/Ni ratio (Kao et al., 2009; Sistla et al., 2015). The other constituents are similarly influencing phase formation such as stabilizing the BCC phase, e.g., Cr (Zhang et al., 2016), or the FCC phase, e.g., Co (Qin et al., 2018). A great number of studies on Al-Co-Cr-Fe-Ni based HEAs showed that mechanical properties, such as hardness (Kao et al., 2009; Wang et al., 2012), tensile and compression strength (Joseph et al., 2017) can be altered by controlling the microstructure through alloying or heat treatment. Furthermore, the corrosion resistance of these alloys can be similar to stainless steel grades such as the austenitic steels (Kuwabara et al., 2018), suggesting the suitability of the alloys for a greater range of applications that require durability in corrosive environments. Such applications can be found in the marine and offshore industry (Nair et al., 2018).

Commonly, in applications where high strength and corrosion resistance are needed, the austenitic, ferritic, and austenitic-ferritic (duplex) steels are used (Nilsson, 1992; Charles, 2008; Aribo et al., 2013; Chai and Kangas, 2017). When compared to stainless steel, HEAs usually contain a large weight percentage of relatively expensive elements such as Co, Cr, and Ni. This certainly is a challenge for the industrialization of these novel alloys and the development of their applications (Yin et al., 2019), and greater focus is needed on the development of cost-effective compositions. While Al-Co-Cr-Fe-Ni based HEAs have been gathering much attention, the Co-free Al-Cr-Fe-Ni system may have comparable properties and a theoretical lower cost. The reported phases, e.g., FCC, BCC, and BCC-B2 and their volume fractions, can be altered by modifying the concentrations of Al and Ni. The mechanical properties can also be modified since they are influenced by the volume fractions of the prescribed phases (Zeng et al., 2018). Jiang et al. showed on an equiatomic cast AlCrFeNi HEA that exhibits mechanical properties such as yield strength higher than 1000 MPa and failure strain greater than 40% (Jiang et al., 2019).

Moreover, an excellent combination of fracture strength and ductility was reported for an as-cast AlCrFe<sub>2</sub>Ni<sub>2</sub> HEA, owing to the combination and morphology of the BCC and FCC phases in the microstructure (Dong et al., 2016). To be precise, the Co-free alloys are rather medium entropy alloys, since their ideal entropy of mixing  $\Delta S_{\text{mix}} = -R \sum_{i=1}^n (x_i \ln x_i)$  ranges from 1R to 1.5R, e.g., 1.33R for AlCrFe<sub>2</sub>Ni<sub>2</sub>. Nevertheless, the distinction is somewhat arbitrary and the HEA concept itself has considerable limitations.

Recently, innovative manufacturing techniques such as Additive Manufacturing (AM) have been utilized for novel alloy processing (Azizi et al., 2018; Li W. et al., 2018; Pozdniakov et al., 2018). Many studies have been focused on the processing of HEAs with AM techniques (Brif et al., 2015; Li R. et al., 2018; Zhang et al., 2019). AM processes offer flexibility in the production of chemically homogenous mixtures from metal powders (Joseph et al., 2015). Laser Powder Bed Fusion (LPBF) is an AM process that offers more advantages related to the final product, such as design freedom and optimized complex shaped parts. Moreover, there are advantages related to the obtained material after processing (as-built material). Microstructures of LPBF processed materials are finer due to fast cooling and exhibit enhanced mechanical properties (Yap et al., 2015).

The current study aimed to process the AlCrFe<sub>2</sub>Ni<sub>2</sub> alloy with LPBF and investigate the influence of the microstructure on the mechanical properties through subsequent heat treatment. The prescribed composition was selected due to its remarkably well-balanced mechanical properties in the as-cast condition and the fact that it is Co-free and therefore a cost-effective solution for structural applications. It was expected that the LPBF processing would further increase the performance of the alloy by obtaining a finer microstructure compared to casting. The heat treatment was used to control the ratio of the formed phases and investigate their impact in the mechanical response of the novel AM material.

## MATERIALS AND METHODS

In the context of the present study, prealloyed powder with composition Al<sub>17.8</sub>Cr<sub>16.4</sub>Fe<sub>33.2</sub>Ni<sub>32.7</sub> close to AlCrFe<sub>2</sub>Ni<sub>2</sub> (Al<sub>16.7</sub>Cr<sub>16.7</sub>Fe<sub>33.3</sub>Ni<sub>33.3</sub>), was produced with gas atomization by Oerlikon Metco. The powder was characterized in terms of chemical composition, particle size distribution (PSD), and morphology. The chemical composition of the powder was measured by Energy Dispersive X-ray Spectroscopy (EDS) using a Zeiss Merlin scanning electron microscope (SEM). Multiple EDS measurements were performed on individual particles and the results were averaged to calculate the powder composition.

**TABLE 1** | LPBF process parameters used for coupon production.

Laser power (W)	Scanning speed (mm/s)	Laser spot size (μm)	Hatch space (μm)	Layer height (μm)
175	1700	80	60	30

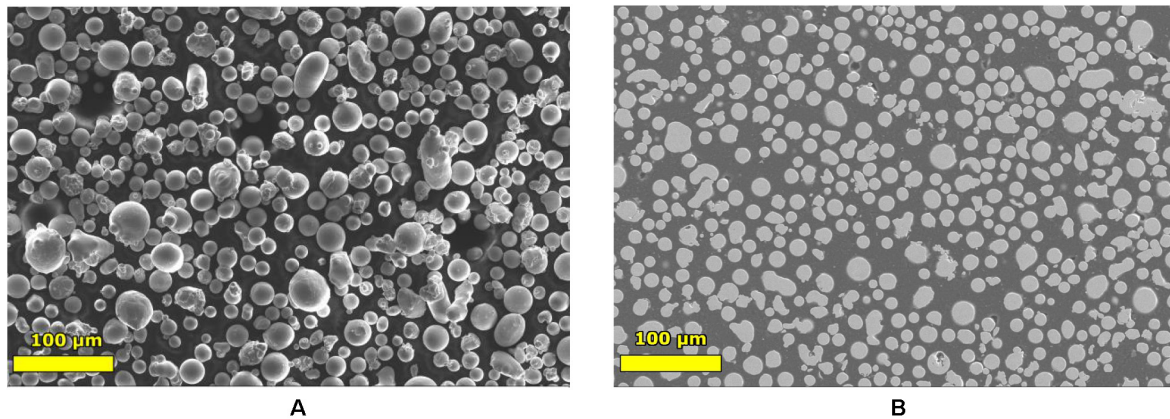


**FIGURE 1** | SEM micrographs of (A) the AlCrFe<sub>2</sub>Ni<sub>2</sub> prealloyed powder particles and (B) cross-section of powder particles.

The powder PSD and morphology were investigated via optical method using a Malvern Morphologi four equipment. For this purpose, powder was sampled from the atomized powder batch and dispersed on a glass plate. Individual optical micrographs of 10000 particles were captured to estimate the PSD based on their diameter. The particle circularity distribution was also estimated as an indication of the sphericity of the powder particles. The circularity of each particle was calculated by the equipment using the following formula:

$$\text{Circularity} = \frac{2 \times \sqrt{\pi \times \text{Area}}}{\text{Perimeter}}$$

The LPBF coupons were built in an Aconity3D MINI machine with a baseplate preheating feature to reduce thermal stresses during the process (Kempen et al., 2014; Mertens et al., 2018). Initial screening builds without baseplate preheating resulted in cracked coupons irrespective of the process parameters. However, process parameters for minimum porosity were developed during the screening builds but will not be discussed further in the current study. Increasing the preheating up to 700°C was needed to obtain bulk material suitable for characterization. The selected process parameters for the build presented in the current study are listed in **Table 1**. A typical meander scanning strategy (Koutny et al., 2018) with a scan vector rotation of 90° per layer was applied. The preheating of the baseplate was kept constant at 700°C during the build and was switched off after the end of the process. The process chamber was filled with argon, while the oxygen content was controlled by the machine and stabilized below 100 ppm. The selected geometry of the coupons was 10 mm × 10 mm × 35 mm blocks. After LPBF processing, the chamber was cooled down to room temperature and the baseplate with the coupons was removed from the printer. The coupons were cut from the baseplate using Wire Electro Discharge Machining (WEDM).

Five coupons were used for post-build annealing heat treatments at 750, 800, 850°C for 3 h and 900, 950°C for 6 h to test the higher temperature and longer treatment time effects on the microstructure. The coupons were heat treated in a

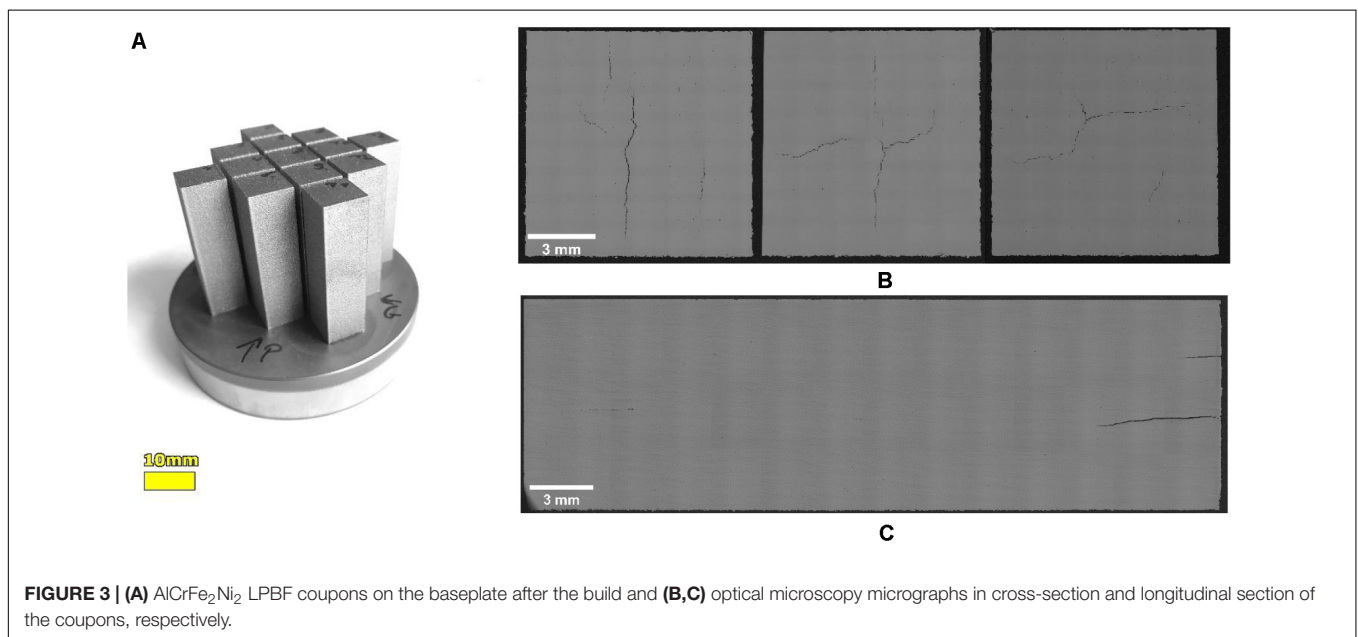
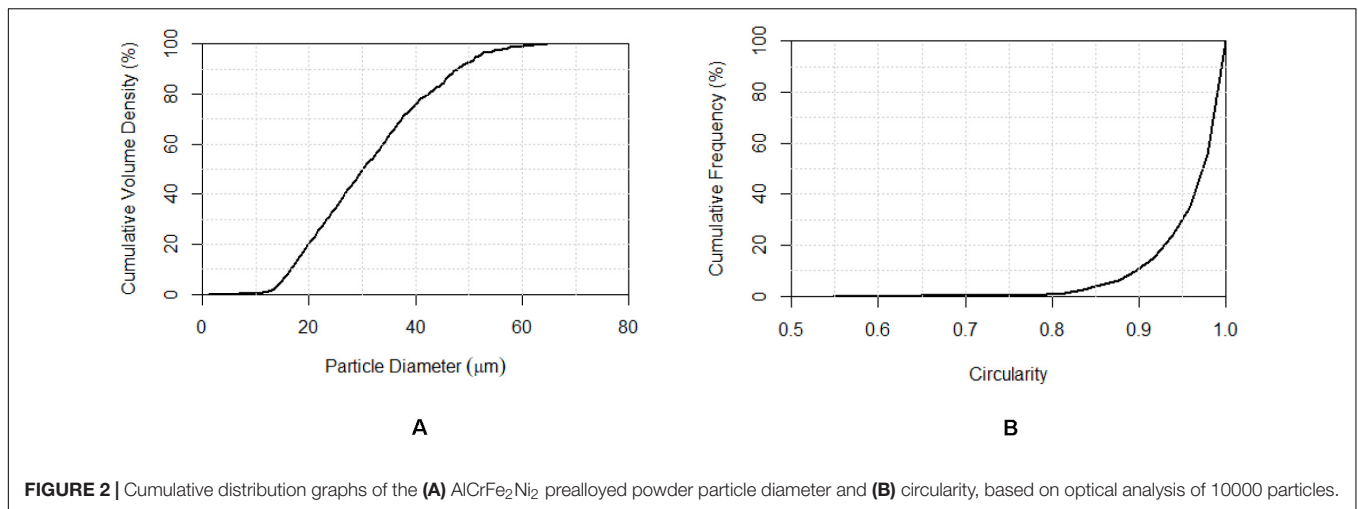
Carbolite Gero CWF 11/13 furnace with a heating rate at 1.1°C/s, under a protective argon atmosphere. After heat treatment, they were left to cool down to room temperature inside the furnace (cooling rate around 0.5°C/s). Thin plate three-point bending specimens with dimensions of 30 mm × 5 mm × 1.6 mm were extracted from the heat treated coupons with WEDM with their length being aligned to the build direction. Before the three-point bending test, the specimens were gently polished to remove surface anomalies. The applied strain rate of the bending test was 0.2 mm/min and the strain limit of the device was 21%. The bending span of the device was 17.2 mm. The microhardness measurements were performed using a Struers DuraScan Microhardness testing equipment with an applied load of 1 kgf.

The porosity levels in the as-built condition were studied using a Zeiss Smartzoom optical microscope by investigating cross-section (perpendicular to build direction) and longitudinal (parallel to build direction) specimens extracted from the coupons. The SEM and Electron Backscatter Diffraction (EBSD) measurements were performed in a Zeiss Merlin and a Zeiss Gemini field emission microscope equipped with backscattered electron detectors.

Postprocessing of the EBSD data was conducted in Matlab® MTEX toolbox for texture and crystallography analysis (Bachmann et al., 2010) and in the Aztec software from Oxford Instruments. Sample preparation for optical microscopy, SEM and EBSD included mechanical grinding down to 4000 μm and subsequent polishing using a diamond paste (1 μm) and a colloidal silica suspension (0.02 μm).

**TABLE 2** | Chemical composition of the powder measured by EDS.

Element	Average (wt.%)	Average (at.%)
Al	9.4 ± 0.2	17.8 ± 0.4
Cr	16.7 ± 0.2	16.4 ± 0.2
Fe	36.3 ± 0.7	33.2 ± 0.6
Ni	37.6 ± 0.7	32.7 ± 0.7



## RESULTS AND DISCUSSION

The overall morphology of the gas atomized AlCrFe<sub>2</sub>Ni<sub>2</sub> powder is shown in **Figure 1A**. As seen, highly spherical particles were observed and few satellites were visible on larger particles. Generally, highly spherical particles are preferred for better powder flow and spreading during the LPBF process. A cross-section SEM micrograph of the particles is shown in **Figure 1B**. No internal defects or inclusions were found in the particles. The chemical composition of the powder measured by EDS on cross-sections of the particles is summarized in **Table 2**. The composition of the powder was found to be matching the nominal composition of the alloy, being slightly higher in Al content and slightly lower in Ni content compared to the baseline AlCrFe<sub>2</sub>Ni<sub>2</sub>. The overall morphology of the powder was further studied via optical imaging. The cumulative frequency distribution of the powder particle diameter can be seen in

**Figure 2A**. From the values that correspond to the 10th (D10) and 90th (D90) percentile, it was estimated that the particle size was ranging between 17 and 48 μm. The presence of fine particles (diameter < 15 μm) did not affect the flowability of the powder during processing. The cumulative distribution graph obtained by optical measurement confirmed that the majority of the particles were highly circular (circularity ≥ 0.9) as seen in **Figure 2B**.

**TABLE 3** | Chemical composition of the LPBF coupons measured by EDS.

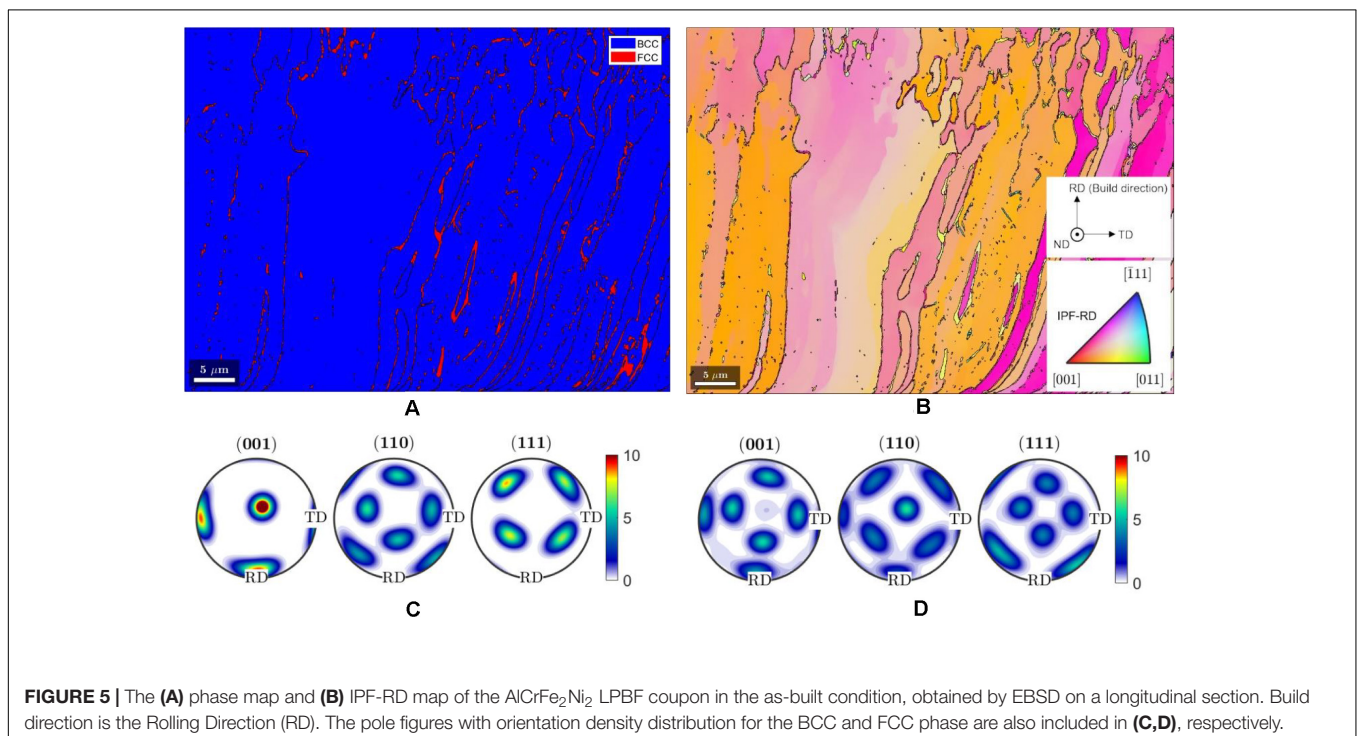
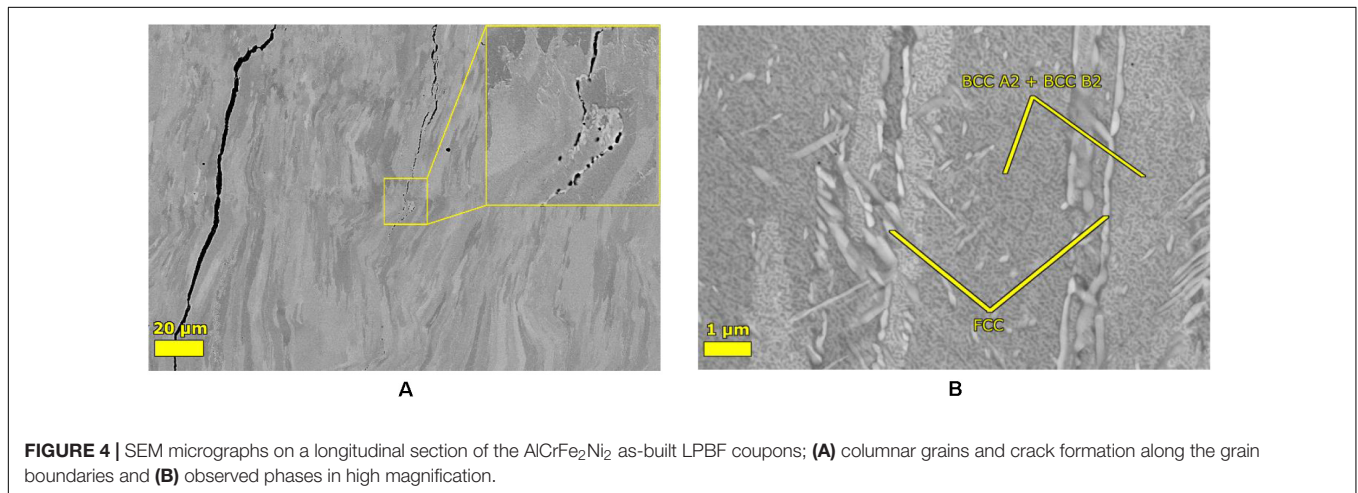
Element	Average (wt.%)	Average (at.%)
Al	9.5 ± 0.1	18.2 ± 0.2
Cr	16.9 ± 0.1	16.5 ± 0.1
Fe	36.4 ± 0.1	33.2 ± 0.2
Ni	37.1 ± 0.2	32.2 ± 0.2

An image of the coupons on the baseplate after LPBF processing can be seen in **Figure 3A**. All coupons were built successfully without noticeable irregularities on the side and top surfaces. Three of them were selected randomly and cross-section specimens were extracted. The specimens were studied using the optical microscope to ensure that they were equivalent in terms of the as-built condition. The corresponding optical microscopy micrographs can be seen in **Figure 3B**. The coupons showed low porosity but exhibited internal cracks. A micrograph taken on a longitudinal specimen can be seen in **Figure 3C**. The cracks were seen to run parallel to the build direction, but no other notable defects were observed. The chemical composition of the specimens was also analyzed. The aim was to ensure that there was no significant deviation from the baseline powder

composition due to potential elemental loss from evaporation during LPBF. The results of the chemical analysis by EDS can be seen in **Table 3**. Based on the given table, and unlike expected, no significant elemental losses were found taking into account the standard error of the EDS measurement.

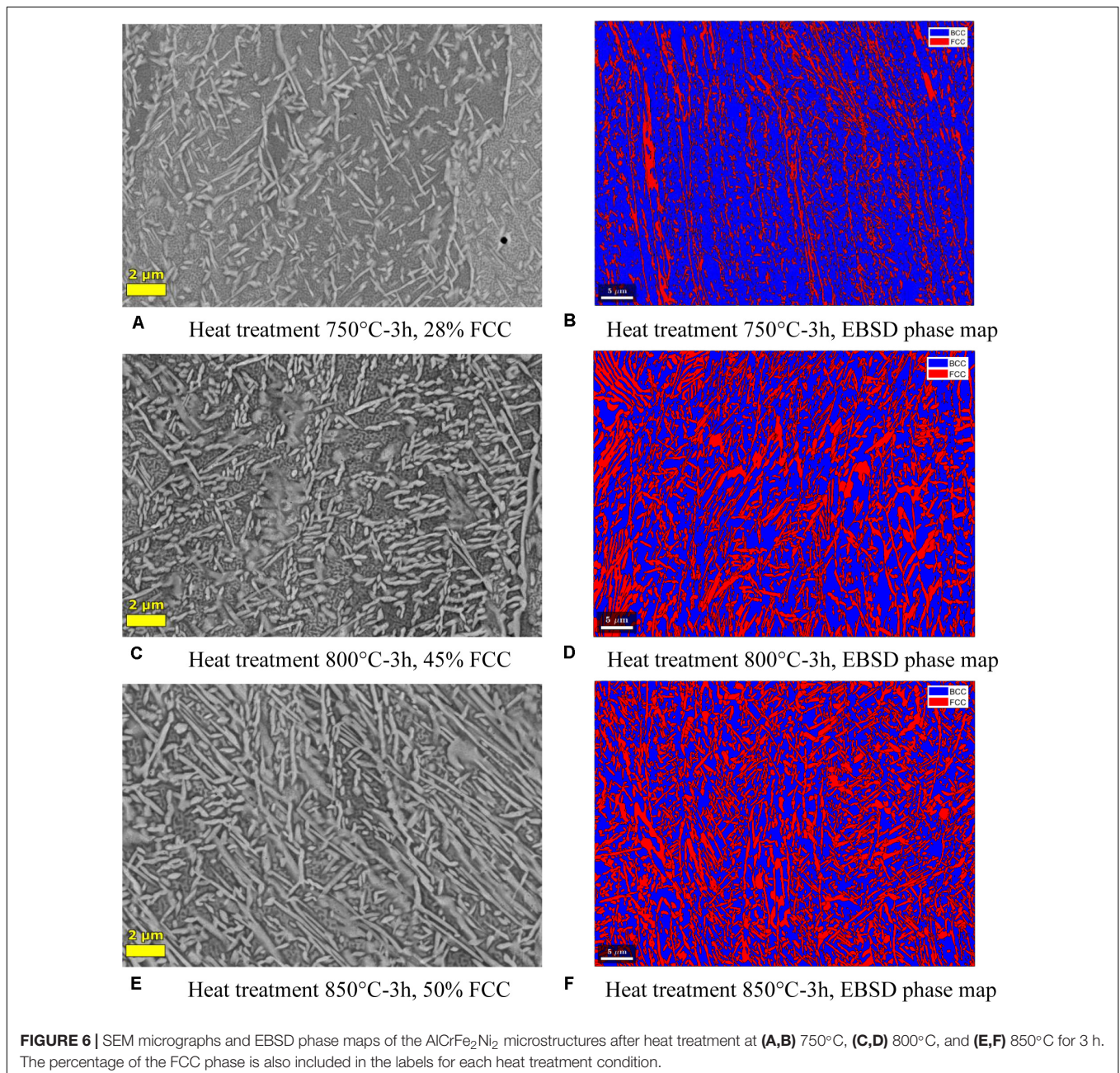
## Microstructural Analysis of the LPBF As-Built AlCrFe<sub>2</sub>Ni<sub>2</sub>

The SEM micrographs obtained from longitudinal sections of as-built blocks can be seen in **Figure 4**. The cracks that were observed under the optical microscope were found to form at intergranular locations, initiating as micro-voids at the grain boundaries as seen in **Figure 4A**. For phase identification,



EBSD was utilized. The diffraction patterns of the columnar grains matched with the iron ferrite phase, while those of the precipitates seen in **Figure 4B** matched with the iron gamma phase, indicating a BCC and an FCC phase, respectively. Most of the secondary phase precipitation was observed mainly in the grain boundaries and only a few intergranular precipitates were present. Apart from the FCC precipitates, at high magnification, a spinodal decomposition (Porter et al., 2009) structure inside the BCC grains was also revealed and can be seen in **Figure 4B**. Similar to previous studies in as-cast AlCrFe<sub>2</sub>Ni<sub>2</sub> (Dong et al., 2016), the brighter precipitate-like features in the spinodal decomposed BCC matrix are disordered, Fe-, Cr-rich A<sub>2</sub>, while

the inter-precipitates seen with gray contrast are ordered B<sub>2</sub>. Compared to the as-cast AlCrFe<sub>2</sub>Ni<sub>2</sub>, in the as-built LPBF microstructure the FCC phase was absent in the volume of the grains. The transformation path of the current HEA is considered similar to that of highly alloyed steels, such as duplex steels (Knyazeva and Pohl, 2013), where initially a ferrite solidification is promoted and on further cooling a diffusion-controlled ferrite to austenite transformation is taking place. However, due to the significantly high cooling rates of the LPBF process (Hooper, 2018; Zhang et al., 2018) the FCC formation is suppressed and limited in the grain boundaries of the parent BCC grains. Thus, the microstructure of the LPBF as-built AlCrFe<sub>2</sub>Ni<sub>2</sub> is



in a metastable state. Secondary phase suppression has been observed in LPBF of other alloys before, e.g., the suppression of austenite in LPBF of duplex steels (Davidson and Singamneni, 2016; Hengsbach et al., 2017) and similar cases of FCC or BCC suppression in LPBF of HEAs such as Al<sub>0.5</sub>CoCrFeNi (Zhou et al., 2019), AlCoCrFeNi (Niu et al., 2019) and AlCoCuFeNi (Zhang et al., 2019).

The phase map of the LPBF as-built condition obtained by EBSD can be seen in **Figure 5A**. Based on the EBSD results, the as-built microstructure consisted of mainly the BCC phase (95%) with a pronounced growth texture. Elongated FCC structures were observed mainly along the parent BCC grain boundaries. The texture of the BCC grains was influenced by the directional heat transfer during the LPBF process. The parent grains grew along the build direction following near <001> orientations as seen in the build direction inverse pole figure (IPF) map in **Figure 5B**. The strong cube texture of the BCC grains can be also seen in the pole figures of the BCC phase, where the highest pole density was found near the <001> orientation, as seen in **Figure 5C**. The FCC pole figures in the as-built condition showed more orientations with higher pole density, as seen in the FCC pole figures of **Figure 5D**. The latter observation indicates the presence of an Orientation Relationship (OR) between the BCC and the FCC phase.

As mentioned earlier, cracks formed at the grain boundaries. Since the microstructure consisted mainly of columnar grains parallel to the build direction, the prolonged grain boundaries could enhance the crack growth. However, with BCC being the high-temperature phase, it is challenging to avoid the columnar grain growth during solidification in LPBF. The epitaxial columnar grain growth along the build direction is common during LPBF and favorable for BCC and FCC metals (Yan et al., 2017). Numerous studies on other BCC and FCC solidifying alloys such as AlCoCrFeNi, AlCoCuFeNi, Inconel 718, and Invar have described the formation of columnar grains parallel to the build direction with LPBF processing (Amato et al., 2012; Qiu et al., 2016; Ni et al., 2017; Niu et al., 2019; Zhang et al., 2019). The cube texture is certainly related to the hatching

strategy (90° scan vector rotation per layer) applied during the build. Alternative rotations such as 67° could avoid the cube texture formation but certainly not the <001> orientation of the parent grains.

## Microstructural Analysis of the Heat Treated AlCrFe<sub>2</sub>Ni<sub>2</sub>

The purpose of the annealing heat treatments was to investigate the evolution of the FCC phase concerning its phase fraction, morphology, crystal OR, and variant selection as well as precipitate size. The spinodally decomposed parent BCC structure obtained by LPBF was expected to greatly increase the nucleation site density for FCC formation during these heat treatments, given the elastic strain energy (coherency stresses) associated with the spinodal interfaces.

The SEM micrographs and EBSD phase maps, given in **Figure 6**, show the microstructure evolution for three heat treatment conditions. After 750°C-3 h heat treatment, FCC precipitates were found to grow at grain boundaries but also inside the spinodally decomposed BCC matrix as seen in **Figures 6A,B**. The FCC fraction increased from 5% (as-built) to 28%. Therefore, it can be concluded that the temperature of the coupons during LPBF did not exceed 750°C for extended periods even with the combined effect of the baseplate preheating and the laser exposure. At higher heat treatment temperatures such as 800°C and 850°C, the FCC phase fraction reached 45 and 50%, respectively. The FCC precipitates were ultrafine platelets, termed microplatelets, as displayed in **Figures 6C–F**. The parent BCC phase retained the spinodal nanostructure, which slightly coarsened.

Heat treatment for longer periods and at higher temperatures revealed slightly different microstructures as displayed in **Figures 7A,B**. The FCC percentage increased to 56 and 63% at 900°C-6 h and 950°C-6 h, respectively. The microplatelets were larger and more homogeneously dispersed in the matrix, while the A2 and B2 spinodal structures of the parent BCC phase were very coarse. In fact, the A2 phase almost vanished after

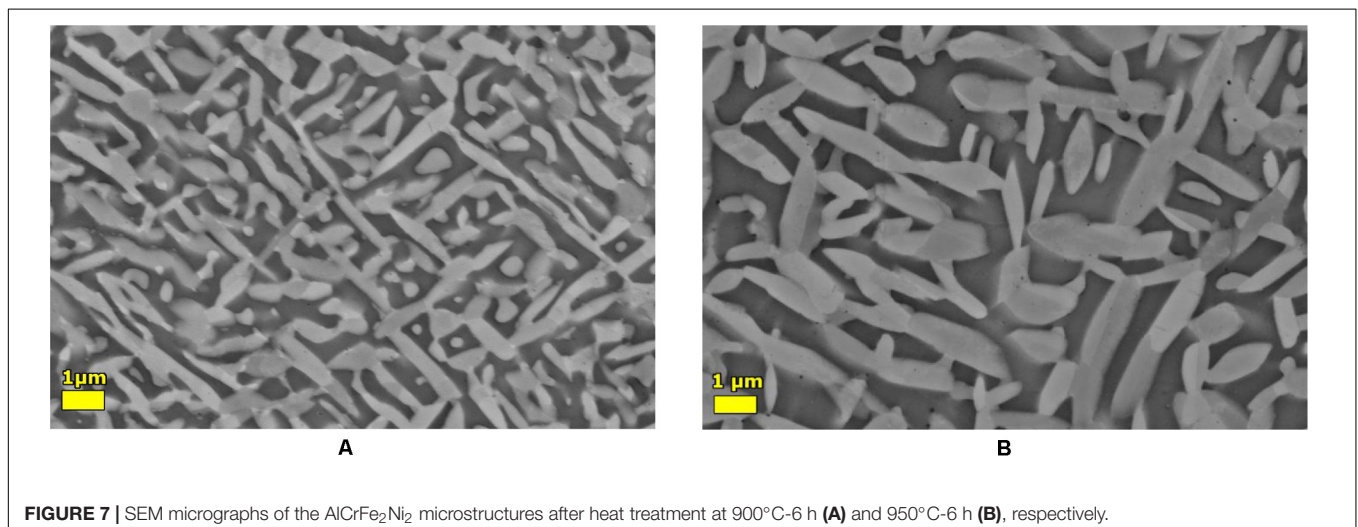


**FIGURE 7** | SEM micrographs of the AlCrFe<sub>2</sub>Ni<sub>2</sub> microstructures after heat treatment at 900°C-6 h (A) and 950°C-6 h (B), respectively.

950°C-6 h treatment. To investigate the OR between the parent BCC phase and the FCC microplatelets, an EBSD analysis was performed inside a single BCC grain of the 950°C-6 h heat treated coupon. The Euler color map in the region of interest is shown in **Figures 8A,B** for the BCC and FCC phases, respectively. The

FCC microplatelets were present in many crystal orientations, which were variants of the crystallographic OR. The variants were homogeneously distributed and no colony formation was observed. From the selected pole figures displayed in **Figure 8C**, it can be concluded that the Nishiyama–Wasserman (N–W) OR

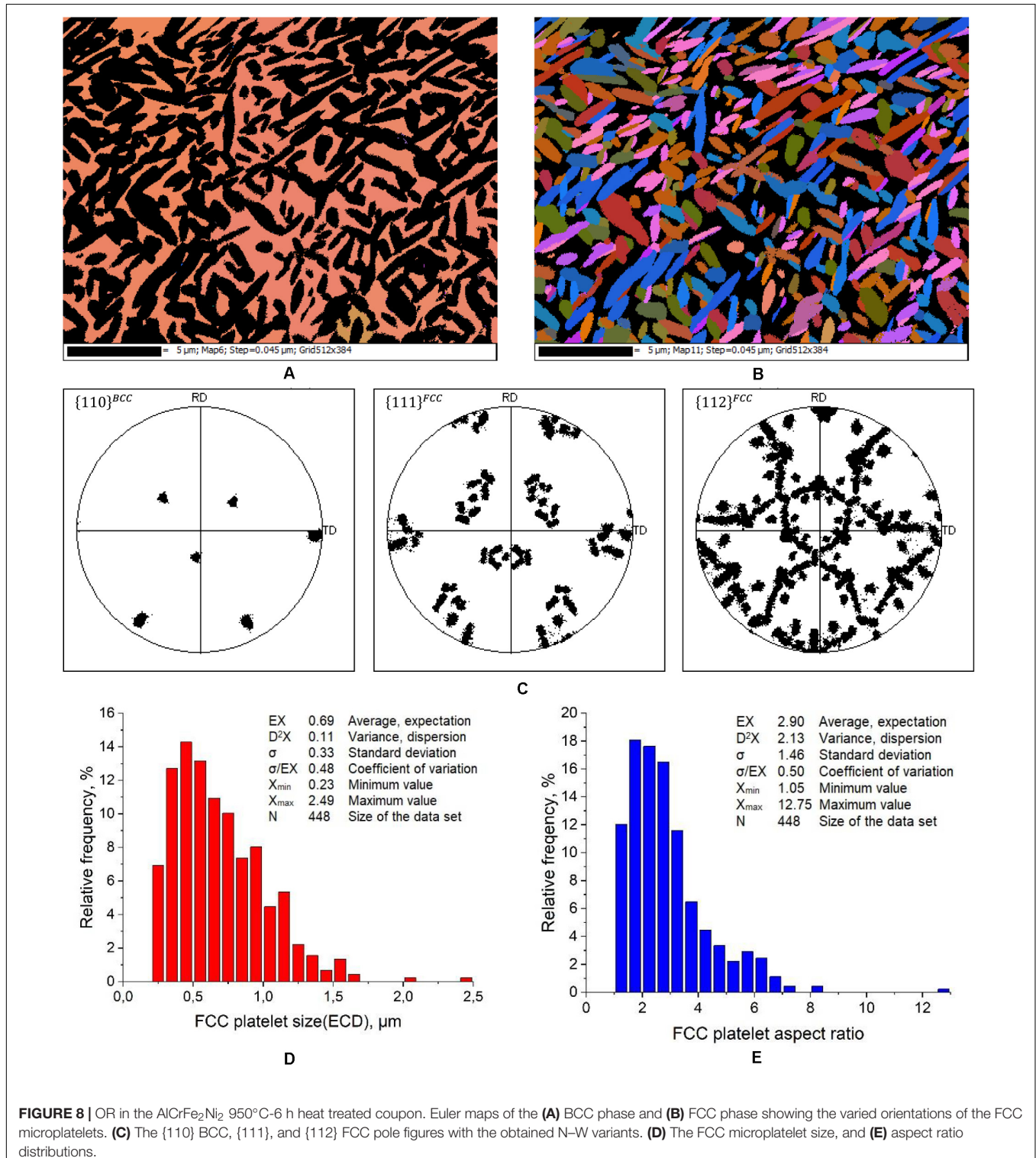


**FIGURE 8** | OR in the AlCrFe<sub>2</sub>Ni<sub>2</sub> 950°C-6 h heat treated coupon. Euler maps of the **(A)** BCC phase and **(B)** FCC phase showing the varied orientations of the FCC microplatelets. **(C)** The  $\{110\}^{BCC}$ ,  $\{111\}^{FCC}$ , and  $\{112\}^{FCC}$  pole figures with the obtained N–W variants. **(D)** The FCC microplatelet size, and **(E)** aspect ratio distributions.

applies and that certainly all of its 12 variants are present. The family of common planes and directions of the N–W OR are:

$$\begin{aligned} & \{111\}^{FCC} \\ & \langle 11\bar{2} \rangle^{FCC} \end{aligned}$$

The full symmetry of the {111} and {112} pole figures is a fingerprint of the fact that all variants are present. This result is remarkable, showing that colony formation and variant selection can be avoided along this transformation pathway, even if FCC is present along grain boundaries in the parent, metastable BCC (as-built). This strongly supports the idea that the spinodal interfaces provide a high number of nucleation sites with a low energy barrier for FCC nucleation. The microplatelet size distribution based on the equivalent circle diameter (ECD), as well as the aspect ratio distribution, can be seen in **Figures 8D,E** for the 950°C-6 h heat treated coupon. The FCC platelets were in the submicron scale and together with the BCC matrix, they formed an ultrafine duplex microstructure. It should be noted that similar pole figures were obtained in the EBSD analysis of a single grain of the 850°C-3 h heat treated coupon, suggesting the presence of all N–W variants already at lower heat treatment temperatures.

The heat treatment study showed that the LPBF process provides unique means to obtain ultrafine or even nanoscale duplex microstructures after heat treatment below 950°C thanks to the formation of FCC platelets from metastable BCC parent grains that have undergone a spinodal decomposition. Prolonged heat treatment at 900°C or higher resulted in significant coarsening of the spinodal structure and partial dissolution of the A2 phase from within the spinodal BCC matrix. The use of a metastable AM microstructure to control the secondary precipitation through subsequent heat treatment is a unique processing path for the AlCrFe<sub>2</sub>Ni<sub>2</sub> HEA.

## Mechanical Properties of the Heat Treated AlCrFe<sub>2</sub>Ni<sub>2</sub>

The mechanical response of the heat treated specimens (30 mm × 5 mm × 1.6 mm) was studied via three-point bending tests. Given the small thickness required for the test specimens crack-free material was extracted by WEDM. The extracted specimens were visually inspected before testing to ensure the absence of cracks. The obtained flexural stress-strain curves are presented in **Figure 9A**. The presented curves are averages from at least three tests. The HEA was not tested in the as-built condition, due to early brittle failure. A super duplex steel (EN 1.4517) was tested as reference material. The curves presented an elastic region followed by plastic deformation with significant work hardening. Compared to the reference material, the heat treated HEA specimens showed significant strain hardening ability and higher flexural strength. However, the super duplex steel showed slightly greater flexural proof stress (1031 MPa) compared to the 900°C-6 h (985 MPa) and 950°C-6 h (851 MPa) heat treated HEA specimens. The 750°C-3 h and 800°C-3 h heat treated specimens showed flexural strength as high as ~3000 and 2800 MPa but failed relatively early during the test, at fracture strains of 10–16%. The 850°C-3 h heat treated specimen retained

high flexural strength at 2805 MPa and exhibited greater fracture strain at 18.9%. However, the fracture strain was much lower than the reference material which did not fail and reached the strain limit of the testing device (21%). The 900°C-6 h heat treated specimens exhibited the best combination of flexural strength and strain among all tested conditions. The calculated flexural strength was 2051 MPa and the specimen reached the strain limit of the device without failing, while the super duplex steel specimen showed significantly lower flexural strength at 1632 MPa without failing. Therefore, it can be said that the 900°C-6 h annealing heat treatment led to the AlCrFe<sub>2</sub>Ni<sub>2</sub> outperforming the reference material in terms of flexural strength in the three-point bending test. However, since those specimens did not fail during the test and exceeded the strain limit of the device, their ductility cannot be directly compared. As of the 950°C-6 h heat treated specimen, a significant decrease in flexural strength was observed compared to the 900°C-6 h. The specimen did not fail during the test but did not exceed the flexural strength of the reference material considerably. The decrease in strength observed in the 950°C-6 h heat treated specimen could be attributed to the coarsening of the microstructure, specifically the coarsening of the spinodal structure inside the BCC matrix along with a partial dissolution of the A2 phase which was described in section “Microstructural Analysis of the Heat Treated AlCrFe<sub>2</sub>Ni<sub>2</sub>”.

Based on the obtained curves from all conditions and the phase fractions obtained by EBSD for the HEA specimens, it was seen that the increase of the FCC phase fraction in the microstructure also increased the ductility while decreasing the flexural strength. The specimens that were heat treated at lower temperatures and less time (750, 800, and 850°C-3 h) retained the spinodal decomposition of the BCC phase in their microstructure and exhibited remarkably high flexural strength. However, they underwent early failure in the test. Longer annealing times at higher temperatures led to microstructures with excessively coarse spinodal structure and the Fe-, Cr- rich A2 phase being partially dissolved. Optimum parameters for an annealing heat treatment thus range from 850 to 900°C for durations from 3 to 6 h, followed by air cooling or furnace cooling. Without being shown here in detail it is important to remark that ideally specimens should be introduced into the preheated furnace or heated up as rapidly as possible to the nominal annealing temperature. These procedures ensure that all nucleation sites are exploited at best and with an equal driving force, which leads to a homogeneous microstructure.

The heat treated specimens were also tested for microhardness. The microhardness values and the FCC percentage in the microstructure of each specimen can be seen in **Figure 9B**. Increased FCC percentage in the microstructure resulted in a decrease in the hardness. However, the hardness of the AlCrFe<sub>2</sub>Ni<sub>2</sub> was higher compared to the reference material for all tested conditions. From the AlCrFe<sub>2</sub>Ni<sub>2</sub> measurements, the 950°C-6 h specimen exhibited the lowest hardness at 303 HV and the highest FCC percentage at 63% in the microstructure. A detailed overview of the flexural and hardness properties obtained from the tests and the respective phase fractions in the microstructures measured by EBSD is presented in **Table 4**.

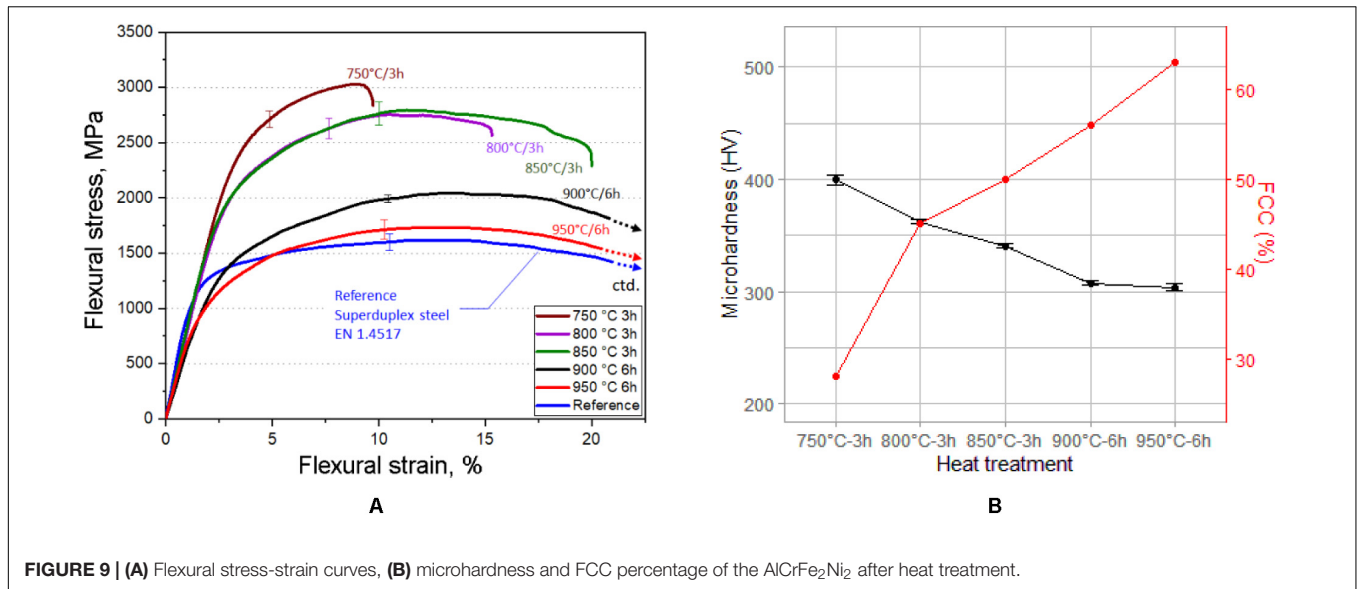


**TABLE 4 |** Mechanical properties based on three-point bending and microhardness tests, including phase percentages in the microstructure measured by EBSD.

Coupon	BCC%	FCC%	Proof stress Rp.02 (MPa)	Flexural strength (MPa)	Flexural strain (%)	Hardness (HV1)
As-built	95	5				483 ± 8
750°C 3 h	72	28	2108 ± 141	3046 ± 99	10.9 ± 1.2	399 ± 5
800°C 3 h	55	45	1785 ± 22	2760 ± 82	16.5 ± 1.3	362 ± 2
850°C 3 h	50	50	1691 ± 47	2805 ± 94	18.9 ± 1.1	341 ± 2
900°C 6 h	44	56	985 ± 47	2051 ± 24	>21	307 ± 2
950°C 6 h	37	63	851 ± 52	1735 ± 73	>21	304 ± 3
EN 1.4517	38	62	1031 ± 70	1633 ± 76	>21	276 ± 2

## CONCLUSION

In this study, a Co-free alloy with a composition close to AlCrFe<sub>2</sub>Ni<sub>2</sub> was prepared by LPBF for the first time to the best of the authors' knowledge. A major issue in the LPBF processing of AlCrFe<sub>2</sub>Ni<sub>2</sub> was cracking that was observed in intergranular sites. However, dense specimens suitable for mechanical testing such as three-point bending and microhardness were successfully obtained with baseplate preheating to mitigate thermo-mechanical stresses. The alloy retained a metastable structure in the as-built condition, mainly consisting of a spinodally decomposed BCC phase. Distinct heat treatment conditions were applied to investigate the precipitation of the FCC phase from the parent BCC and its influence on mechanical properties. The following conclusions are presented:

- (i) Prealloyed HEA powder can be atomized based on the AlCrFe<sub>2</sub>Ni<sub>2</sub> composition with spherical particles and PSD suitable for LPBF processing.
- (ii) Processing the AlCrFe<sub>2</sub>Ni<sub>2</sub> with LPBF requires high preheating of the baseplate to obtain bulk material suitable for mechanical testing.
- (iii) The microstructure of the as-built AlCrFe<sub>2</sub>Ni<sub>2</sub> is metastable. It consists of columnar BCC grains with nanoscale spinodal decomposition B2 and A2 structures and grains that are parallel to the build direction with near <001> texture. For the applied hatching strategy and build parameters, a cube texture is expected.
- (iv) Based on the observations from the heat treatment studies, increasing the treatment temperature and time allows reaching equilibrium values (i.e., 63% FCC), while FCC fractions remain below the equilibrium values if temperature and/or time are too low. Notably, the FCC phase is precipitating as microplatelets, thus leading to an ultrafine and homogeneous duplex microstructure. Furthermore, the FCC microplatelets display all crystal orientations compatible with the N-W OR. All crystallographic variants are present and randomly distributed, such that the overall texture is mitigated. Colony formation is suppressed because the spinodal structure of the parent BCC provides a high density of nucleation sites.
- (v) The optimum annealing heat treatment parameters range from 850 to 900°C for 3 to 6 h. In these conditions, the HEA's strength is superior to the super-duplex steel EN 1.4517, while a good balance between strength and ductility is achieved. Further mechanical and corrosion tests are due to characterize the property profile and envisage application cases.

## DATA AVAILABILITY STATEMENT

The raw data supporting the conclusions of this article will be made available by the authors, without undue reservation.

## AUTHOR CONTRIBUTIONS

DV designed the experiments, analyzed the powder, the bulk material, and the results obtained from all measurements and tests presented in this manuscript. AE carried out EBSD measurements and took part in the SEM investigation. MP contributed to the planning of the work and supervision of the actions. SG carried out the three-point bending tests. VM and AW carried out screening builds toward baseplate preheating temperature selection.

## REFERENCES

- Amato, K. N., Gaytan, S. M., Murr, L. E., Martinez, E., Shindo, P. W., Hernandez, J., et al. (2012). Microstructures and mechanical behavior of Inconel 718 fabricated by selective laser melting. *Acta Mater.* 60, 2229–2239. doi: 10.1016/j.actamat.2011.12.032
- Aribo, S., Barker, R., Hu, X., and Neville, A. (2013). Erosion-corrosion behaviour of lean duplex stainless steels in 3.5% NaCl solution. *Wear* 302, 1602–1608. doi: 10.1016/j.wear.2012.12.007
- Azizi, H., Zurob, H., Bose, B., Reza Ghiaasiaan, S., Wang, X., Coulson, S., et al. (2018). Additive manufacturing of a novel Ti-Al-V-Fe alloy using selective laser melting. *Addit. Manuf.* 21, 529–535. doi: 10.1016/j.addma.2018.04.006
- Bachmann, F., Hielscher, R., and Schaeben, H. (2010). Texture analysis with MTEX- Free and open source software toolbox. *Solid State Phenom.* 160, 63–68. doi: 10.4028/www.scientific.net/ssp.160.63
- Brif, Y., Thomas, M., and Todd, I. (2015). The use of high-entropy alloys in additive manufacturing. *Scr. Mater.* 99, 93–96. doi: 10.1016/j.scriptamat.2014.11.037
- Chai, G., and Kangas, P. (2017). Recent developments of advanced austenitic and duplex stainless steels for oil and gas industry. *Energy Mater.* 2014, 703–709. doi: 10.1007/978-3-319-48765-6\_85
- Charles, J. (2008). Duplex stainless steels, a review after DSS'07 in Grado. *Rev. Metallurgie* 105, 155–171. doi: 10.1051/metal:2008028
- Davidson, K., and Singamneni, S. (2016). Selective laser melting of duplex stainless steel powders: an investigation. *Mater. Manuf. Process.* 31, 1543–1555 doi: 10.1080/10426914.2015.1090605
- Dong, Y., Gao, X., Lu, Y., Wang, T., and Li, T. (2016). A multi-component AlCrFe2Ni2 alloy with excellent mechanical properties. *Mater. Lett.* 169, 62–64. doi: 10.1016/j.matlet.2016.01.096
- Hengsbach, F., Koppa, P., Duschik, K., Holzweissig, M. J., Burns, M., Nellesen, J., et al. (2017). Duplex stainless steel fabricated by selective laser melting - Microstructural and mechanical properties. *Mater. Des.* 133, 136–142. doi: 10.1016/j.matdes.2017.07.046
- Hooper, P. A. (2018). Melt pool temperature and cooling rates in laser powder bed fusion. *Addit. Manuf.* 22, 548–559. doi: 10.1016/j.addma.2018.05.032
- Jiang, Z., Chen, W., Xia, Z., Xiong, W., and Fu, Z. (2019). Influence of synthesis method on microstructure and mechanical behavior of Co-free AlCrFeNi medium-entropy alloy. *Intermetallics* 108, 45–54. doi: 10.1016/j.intermet.2019.02.006
- Joseph, J., Jarvis, T., Wu, X., Stanford, N., Hodgson, P., and Fabijanic, D. M. (2015). Comparative study of the microstructures and mechanical properties of direct laser fabricated and arc-melted AlxCoCrFeNi high entropy alloys. *Mater. Sci. Eng. A* 633, 184–193. doi: 10.1016/j.msea.2015.02.072
- Joseph, J., Stanford, N., Hodgson, P., and Fabijanic, D. M. (2017). Understanding the mechanical behaviour and the large strength/ductility differences between FCC and BCC AlxCoCrFeNi high entropy alloys. *J. Alloys Compd.* 726, 885–895. doi: 10.1016/j.jallcom.2017.08.067

All authors contributed to the article and approved the submitted version.

## FUNDING

This research was supported by the German Federal Ministry for Education and Research (BMBF) under grant number 03XP0163D in the frame of the M-era.Net Joint Call 2017, Project NADEA (no. 5129).

## ACKNOWLEDGMENTS

The authors kindly thank Otto Junker GmbH for providing the super-duplex steel EN 1.4517 (ASTM A890 Grade 1C) in the cast and fully heat treated condition to serve as reference material.

- Kao, Y.-F., Chen, T.-J., Chen, S.-K., and Yeh, J.-W. (2009). Microstructure and mechanical property of as-cast, -homogenized, and -deformed AlxCoCrFeNi (0=x=2) high-entropy alloys. *J. Alloys Compd.* 488, 57–64. doi: 10.1016/j.jallcom.2009.08.090
- Kempen, K., Vrancken, B., Bults, S., Thijs, L., Van Humbeeck, J., and Kruth, J.-P. (2014). Selective laser melting of crack-free high density M2 high speed steel parts by baseplate preheating. *J. Manuf. Sci. Eng.* 136:061026. doi: 10.1115/1.4028513
- Knyazeva, M., and Pohl, M. (2013). Duplex steels: part i: genesis, formation, structure. *Metallogr. Microstruct. Anal.* 2, 113–121. doi: 10.1007/s13632-013-0066-8
- Koutny, D., Palousek, D., Pantelejev, L., Hoeller, C., Pichler, R., Tesicky, L., et al. (2018). Influence of scanning strategies on processing of aluminum alloy EN AW 2618 using selective laser melting. *Materials* 11:298. doi: 10.3390/ma11020298
- Kuwabara, K., Shiratori, H., Fujieda, T., Yamanaka, K., Koizumi, Y., and Chiba, A. (2018). Mechanical and corrosion properties of AlCoCrFeNi high-entropy alloy fabricated with selective electron beam melting. *Addit. Manuf.* 23, 264–271. doi: 10.1016/j.addma.2018.06.006
- Li, R., Niu, P., Yuan, T., Cao, P., Chen, C., and Zhou, K. (2018). Selective laser melting of an equiatomic CoCrFeMnNi high-entropy alloy: processability, non-equilibrium microstructure and mechanical property. *J. Alloys Compd.* 746, 125–134. doi: 10.1016/j.jallcom.2018.02.298
- Li, W., Chen, X., Yan, L., Zhang, J., Zhang, X., and Liou, F. (2018). Additive manufacturing of a new Fe-Cr-Ni alloy with gradually changing compositions with elemental powder mixes and thermodynamic calculation. *Int. J. Adv. Manuf. Technol.* 95, 1013–1023. doi: 10.1007/s00170-017-1302-1
- Mertens, R., Dadbakhsh, S., Van Humbeeck, J., and Kruth, J. P. (2018). Application of base plate preheating during selective laser melting. *Proc. CIRP* 74, 5–11. doi: 10.1016/j.procir.2018.08.002
- Miracle, D. B., and Senkov, O. N. (2017). A critical review of high entropy alloys and related concepts. *Acta Mater.* 122, 448–511. doi: 10.1016/j.actamat.2016.08.081
- Nair, R. B., Arora, H. S., Mukherjee, S., Singh, S., Singh, H., and Grewal, H. S. (2018). Exceptionally high cavitation erosion and corrosion resistance of a high entropy alloy. *Ultrason. Sonochem.* 41, 252–260. doi: 10.1016/j.ulsonch.2017.09.044
- Ni, M., Chen, C., Wang, X., Wang, P., Li, R., Zhang, X., et al. (2017). Anisotropic tensile behavior of in situ precipitation strengthened Inconel 718 fabricated by additive manufacturing. *Mater. Sci. Eng. A* 701, 344–351. doi: 10.1016/j.msea.2017.06.098
- Nilsson, J.-O. (1992). Super duplex stainless steels. *Mater. Sci. Technol.* 8, 685–700. doi: 10.1179/mst.1992.8.8.685
- Niu, P. D., Li, R. D., Yuan, T. C., Zhu, S. Y., Chen, C., Wang, M. B., et al. (2019). Microstructures and properties of an equimolar AlCoCrFeNi high entropy alloy printed by selective laser melting. *Intermetallics* 104, 24–32. doi: 10.1016/j.intermet.2018.10.018

- Poletti, M. G., Fiore, G., Gili, F., Mangherini, D., and Battezzati, L. (2017). Development of a new high entropy alloy for wear resistance: FeCoCrNiW0.3 and FeCoCrNiW0.3 + 5 at.% of C. *Mater. Des.* 115, 247–254. doi: 10.1016/j.matdes.2016.11.027
- Porter, D. A., Easterling, K. E., and Sherif, M. Y. (2009). *Phase Transformations in Metals and Alloys, Third Edition*. Cheltenham: Nelson Thornes Ltd.
- Pozdniakov, A. V., Churyumov, A. Y., Loginova, I. S., Daubarayte, D. K., Ryabov, D. K., and Korolev, V. A. (2018). Microstructure and properties of novel AlSi11CuMn alloy manufactured by selective laser melting. *Mater. Lett.* 225, 33–36. doi: 10.1016/j.matlet.2018.04.077
- Qin, G., Xue, W., Fan, C., Chen, R., Wang, L., Su, Y., et al. (2018). Effect of Co content on phase formation and mechanical properties of (AlCoCrFeNi)<sub>100-x</sub>Cox high-entropy alloys. *Mater. Sci. Eng. A* 710, 200–205. doi: 10.1016/j.msea.2017.10.088
- Qiu, C., Adkins, N. J. E., and Attallah, M. M. (2016). Selective laser melting of Invar 36: microstructure and properties. *Acta Mater.* 103, 382–395. doi: 10.1016/j.actamat.2015.10.020
- Sistla, H. R., Newkirk, J. W., and Frank Liou, F. (2015). Effect of Al/Ni ratio, heat treatment on phase transformations and microstructure of Al<math>x</math>/FeCoCrNi<math>2-x</math> (x=0.3, 1) high entropy alloys. *Mater. Des.* 81, 113–121. doi: 10.1016/j.matdes.2015.05.027
- Wang, W. R., Wang, W. L., Wang, S. C., Tsai, Y. C., Lai, C. H., and Yeh, J. W. (2012). Effects of Al addition on the microstructure and mechanical property of Al xCoCrFeNi high-entropy alloys. *Intermetallics* 26, 44–51. doi: 10.1016/j.intermet.2012.03.005
- Yan, F., Xiong, W., and Faierson, E. J. (2017). Grain structure control of additively manufactured metallic materials. *Materials* 10:1260. doi: 10.3390/ma10111260
- Yap, C. Y., Chua, C. K., Dong, Z. L., Liu, Z. H., Zhang, D. Q., Loh, L. E., et al. (2015). Review of selective laser melting: materials and applications. *Appl. Phys. Rev.* 2:041101. doi: 10.1063/1.4935926
- Yeh, J.-W. (2006). Recent progress in high-entropy alloys. *Ann. Chim. Sci. des Matériaux* 31, 633–648. doi: 10.3166/acsm.31.633-648
- Yeh, J. W., Chen, S. K., Lin, S. J., Gan, J. Y., Chin, T. S., Shun, T. T., et al. (2004). Nanostructured high-entropy alloys with multiple principal elements: novel alloy design concepts and outcomes. *Adv. Eng. Mater.* 6, 299–303. doi: 10.1002/adem.200300567
- Yin, Y., Zhang, J., Tan, Q., Zhuang, W., Mo, N., Bermingham, M., et al. (2019). Novel cost-effective Fe-based high entropy alloys with balanced strength and ductility. *Mater. Des.* 162, 24–33. doi: 10.1016/j.matdes.2018.11.033
- Zeng, J., Wu, C., Peng, H., Liu, Y., Wang, J., and Su, X. (2018). Microstructure and microhardness of as-cast and 800°C annealed Al<sub>x</sub>Cr<sub>0.2</sub>Fe<sub>0.2</sub>Ni<sub>0.6-x</sub> and Al<sub>0.2</sub>Cr<sub>0.2</sub>Fe<sub>y</sub>Ni<sub>0.6-y</sub> alloys. *Vacuum* 152, 214–221. doi: 10.1016/j.vacuum.2018.03.035
- Zhang, C., Zhang, F., Diao, H., Gao, M. C., Tang, Z., Poplawsky, J. D., et al. (2016). Understanding phase stability of Al-Co-Cr-Fe-Ni high entropy alloys. *Mater. Des.* 109, 425–433. doi: 10.1016/j.matdes.2016.07.073
- Zhang, D., Feng, Z., Wang, C., Wang, W., Liu, Z., and Niu, W. (2018). Comparison of microstructures and mechanical properties of Inconel 718 alloy processed by selective laser melting and casting. *Mater. Sci. Eng. A* 724, 357–367. doi: 10.1016/j.msea.2018.03.073
- Zhang, M., Zhou, X., Wang, D., Zhu, W., Li, J., and Zhao, Y. F. (2019). AlCoCuFeNi high-entropy alloy with tailored microstructure and outstanding compressive properties fabricated via selective laser melting with heat treatment. *Mater. Sci. Eng. A* 743, 773–784. doi: 10.1016/j.msea.2018.11.118
- Zhou, P. F., Xiao, D. H., Wu, Z., and Ou, X. Q. (2019). Al<sub>0.5</sub>FeCoCrNi high entropy alloy prepared by selective laser melting with gas-atomized pre-alloy powders. *Mater. Sci. Eng. A* 739, 86–89. doi: 10.1016/j.msea.2018.10.035
- Zhou, Y. J., Zhang, Y., Wang, Y. L., and Chen, G. L. (2007). Microstructure and compressive properties of multicomponent Al<sub>x</sub>(TiVCrMnFeCoNiCu)<sub>100-x</sub> high-entropy alloys. *Mater. Sci. Eng. A* 454–455, 260–265. doi: 10.1016/j.msea.2006.11.049

**Conflict of Interest:** DV, AE, and MP were employed by the company Oerlikon AM GmbH.

The remaining authors declare that the research was conducted in the absence of any commercial or financial relationships that could be construed as a potential conflict of interest.

Copyright © 2020 Vogiatzief, Evirgen, Gein, Molina, Weisheit and Pedersen. This is an open-access article distributed under the terms of the Creative Commons Attribution License (CC BY). The use, distribution or reproduction in other forums is permitted, provided the original author(s) and the copyright owner(s) are credited and that the original publication in this journal is cited, in accordance with accepted academic practice. No use, distribution or reproduction is permitted which does not comply with these terms.